Magnetically induced CO2 methanation in continuous flow over supported nickel catalysts with improved energy efficiency

Sourav Ghosh, Thibault Ourlin, Pier-Francesco Fazzini, Lise-Marie Lacroix, Simon Tricard, Jérôme Esvan, Simon Cayez, Bruno Chaudret

10.1002/cssc.202201724

Magnetically induced CO_2 methanation in continuous flow over supported nickel catalysts with improved energy efficiency

Sourav Ghosh,[a],‡, Thibault Ourlin[a],‡ Pier-Francesco Fazzini,[a] Lise-Marie Lacroix,[a] Simon Tricard,[a] Jerome Esvan,[b] Simon Cayez,[a] and Bruno Chaudret[a],**

[a] Dr. S. Ghosh, T. Ourlin, Dr. P.-F. Fazzini, Dr. L.-M. Lacroix, Dr. S. Tricard, S. Cayez, Prof. Dr. B. Chaudret

LPCNO (Laboratoire de Physique et Chimie des Nano-Objets), Université de Toulouse, CNRS, INSA, UPS, 31077 Toulouse, France.

Email: chaudret@insa-toulouse.fr; ghosh@insa-toulouse.fr

[b] J. Esvan

CIRIMAT-ENSIACET, INP-ENSIACET, 4 allée Emile Monso, BP 44362, 31030 Toulouse cedex 4, France.

ABSTRACT: Here we report a new selective and efficient catalytic system for magnetically induced catalytic CO_2 methanation composed of an abundant iron-based heating agent, namely a commercial iron wool, combined with supported Nickel nanoparticles (Ni NPs) as catalysts. The effect of metal oxide support was evaluated by preparing different 10wt% Ni catalyst (TiO_2, ZrO_2, CeO_2, and $CeZrO_2$) via organometallic decomposition route. As prepared catalysts were thoroughly characterized using powder X-ray diffraction, electron microscopy, elemental analysis, vibrating sample magnetometer, and X-ray photoelectron spectroscopy techniques. High conversion and selectivity toward methane were observed at mid-temperature range, hence, improving energy efficiency of the process with respect to the previous results under magnetic heating conditions. To gain further insight into the catalytic system, the effects of the synthesis method and of 0.5wt% Ru doping were evaluated. Finally, the dynamic nature of magnetically induced heating was demonstrated through fast stop-and-go experiments, proving the suitability of this technology for the storage of intermittent renewable energy through P2G process.

KEYWORDS: energy efficiency, heterogeneous catalysis, magnetically induced catalysis, power-to-gas, supported catalysts.

Introduction

The constantly increasing CO_2 emissions and the imminent depletion of fossil resources has led the world organizations to agree on new strategies to supply the global energy demand in a greener and more sustainable way.[1] Since cutting CO_2 emissions to zero seems today impossible, it appears necessary that the chemical industry would have to play a key role in the CO_2

valorization.[2] In that prospect, the integration of the century-old Sabatier reaction in power-to-gas (P2G) processes has recently ascended as a possible outcome. In such a process, water electrolysis-generated H_2 produced with renewable electricity excess would be used to hydrogenate CO_2 into methane, the storage and transportation of which has been established for a long time.[3-5] Herein, the process has been schematically shown in scheme 1.

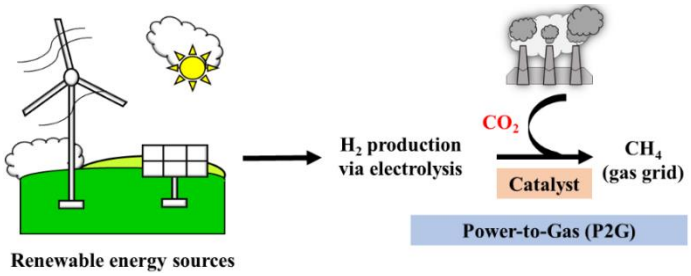

Scheme 1. Pictorial depiction of power-to-gas (P2G) process.

One of the main challenges constraining the conventional P2G process is the intrinsic intermittency of renewable energies.[6] It implies that any technology that would be used to hydrogenate CO_2 must display high dynamicity and efficiency to fully convert the hydrogen while it's available. However, in heterogeneous catalysis, the typical joule-heating mediated processes need high heating time (slow temperature ramp) to reach the desired reaction temperature. To address this issue, we have dedicated many efforts in the past years in our group to develop magnetic heating as an alternative way to heat catalytic systems in much more efficient and faster way.

This technology relies on the fact that ferromagnetic and electrical conductor materials will release heat through hysteresis losses and eddy currents generation whenever immersed in an

alternating magnetic field.[7] Such magnetic heating is both a well-established mode of heating, for instance in the contact-less pre-heating of steel billet in the iron industry,[8] and also a promising field of research, typically in the case of magnetic nanoparticles (MNPs) hyperthermia for the cancer treatment field.[9] In heterogeneous catalysis, it was previously shown that this in-situ generated heat could be successfully used to trigger catalytic reactions such as Fischer-Tropsch,[10] CO_2 methanation,[11,12] methane dry reforming,[13-15] propane dehydrogenation,[13] as well as reactions in solution such as C-O cleavage of ethers and ketones.[16,17]

The main advantage exploited for the P2G scenario is the dynamic nature of magnetically induced catalysis. Few hundreds of degrees can be reached in few seconds at the very core of the reactor, which avoids unnecessary heating of the whole reactor and furnace, saving both time and energy and therefore being an appropriate response to intermittency.[18] From a catalytic point of view, additional advantages arise from magnetic heating, such as suppression of heat-transfer limitations as a result of localized heating[18] or ease of heat management and reactor design in the case of exothermic reactions.[19] Finally, previous work from our group underlined the high energy efficiency of this mean of heating, as it was proven that magnetic heating required 5 times less power than oven joule-heating to trigger the Sabatier reaction in same conditions and yields of reaction.[20]

Previous experiments have used MNPs as either dual heating-catalytic agent or heating agent only, and it was found that the sintering or agglomeration can lead to a change in the heating power over time,[21] making them in some cases unsuitable for extended use in industrial catalytic systems. Moreover, the chemical synthesis of the aforementioned is complex which translates into significant time and money consumption. Therefore, it appeared necessary to simplify the heating agent involved. A first attempt by Faure *et al.* used microscopic Fe powder and silicon carbide

(SiC) particles as a spacer.[20] However, despite its low heating power, this Fe powder, like magnetic nanoparticles, was shown to sinter in the presence of magnetic induction.[20] One of the main goals of magnetically induced catalysis for Sabatier reaction, if implementation at the industrial scale is considered, is energy efficiency. Furthermore, the process needs to be scalable, cheap and commercially viable. Consequently, the search for new Fe materials was continued in order to find out the suitable heating agent, which would be combined with an optimized Ni based methanation catalyst. In the present study, an iron wool (Fe wool), composed of multiple ~50-100 μm iron microwires, and traditionally used for the abrasive cleaning of surfaces, was used as a heating agent. In spite of its comparatively lower heating power (with respect to MNPs), it is a convenient (air stable and abundant) as well as cheap heating agent. Furthermore, its spongy morphology allows an easy separation from the catalytic powder, and also acts as a spacer, avoiding pressure overload in the reactor.

For the catalytic function, Ni was chosen as an active metal as it is long-time established that it is a reasonable tradeoff between price, activity and methane selectivity for the Sabatier reaction.[22,23] Morphology[24] and dispersion[25,26] of Ni particles is of great interest in the literature, as it is believed that such properties strongly influence catalytic activity, methane selectivity, and stability. In this study, we have synthesized Ni NPs through an organometallic decomposition route, leading to monodisperse in size and homogeneously dispersed NPs. As a point of comparison, typical Ni impregnation method was carried out. It is also well known that metal oxide supports play a key role in the overall activity displayed by the catalyst.[27,28] Amount and strength of acidic/basic sites, reducibility or amount of oxygen vacancies are typical intrinsic properties of metal oxide supports that can be used advantageously to tailor catalyst activity. Therefore, and in order to assess support effects, Ni NPs were synthesized on four different metal oxide supports,

namely TiO_2 (P25), ZrO_2, CeO_2, and $CeZrO_2$, and used as catalysts. Eventually, the effect of Ru doping was assessed, since Ru is known as a more active metal for CO_2 activation.[23,29] The physical mixture of the Fe wool and the supported Ni NPs powder was used as the catalytic bed. Herein, we describe the use of a catalytic system based on commercial Fe wool and Ni catalysts for the selective hydrogenation of CO_2 into methane in the presence of magnetic heating. Energy efficiency of the process, effect of support and synthesis method are assessed.

Results and Discussion

Synthesis and characterization of as prepared catalysts

The supported nickel catalysts (10 wt.%) were prepared by thermal decomposition of the organometallic precursor, $Ni(COD)_2$ at 150°C in mesitylene under argon atmosphere, in the presence of an oxide support (see experimental section for details). The synthetic method is robust and scalable up to gram scale. As prepared supported nickel catalysts were characterized using powder XRD, BET, SEM and SEM-EDS mapping, ICP-AES, BF TEM, STEM-EDS elemental mapping, and VSM techniques. Figure 1 shows the stack plot of the powder XRD patterns of different catalysts. The powder XRD pattern of supported nickel catalysts confirm the respective crystallographic phases of the supports whereas the patterns are devoid of diffraction peaks corresponding to the fcc (face-centered cubic) phase of metallic nickel (the black vertical drop lines in figure 1). The absence of nickel diffraction peaks results from the amorphous nature of the nickel which was further supported by the high-resolution transmission electron microscopy (HRTEM) study and magnetic measurements (further discussed in the following section).

10.1002/cssc.202201724

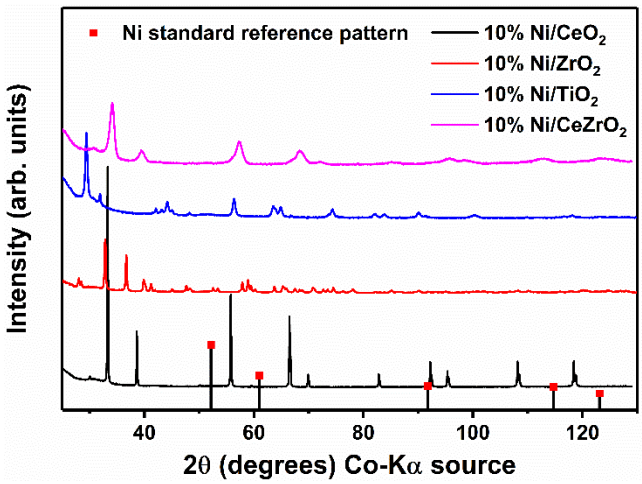

Figure 1. Stack plot of powder XRD patterns of as prepared catalysts; 10%Ni/CeO_2 (ICDD: 00-034-0394), 10%Ni/ZrO_2 (ICDD: 00-037-1484), 10%Ni/$CeZrO_2$ (ICDD: 00-038-1436), and 10%Ni/TiO_2 (ICDD: 00-021-1272 for anatase phase, and 00-021-1276 for rutile phase). Vertical black drop lines correspond to the diffraction peaks of standard fcc bulk Ni (ICDD: 00-004-0850).

Table 1 tabulates the surface area and elemental analysis data of the as prepared supported catalysts. The nickel concentration within the samples were measured by elemental analysis. The ICP-AES measurements confirm the ~10 wt% nickel content for all the catalysts. The surface area of the as prepared catalysts was determined from the nitrogen adsorption-desorption isotherms via applying the BET method. The N_2 adsorption-desorption isotherms are shown on figure S5 (ESI). The BET surface area of the as prepared supported nickel samples is measured to be 20, 15, 71, and 77 $m^2.g^{-1}$ for CeO_2, ZrO_2, $CeZrO_2$ and TiO_2 supports, respectively. The shape of the isotherms is corresponding to the type II, which is typical for macroporous or non-porous solids. The surface area values resemble the macroscopic geometric dimensions of the supports; the relatively large

support particles such as CeO_2 and ZrO_2 exhibit lower surface area than the TiO_2 and $CeZrO_2$ supports, whose particles size are comparatively smaller.

Table 1. Surface area and elemental analysis of the as prepared catalyst, and comparison of Ni particles size before and after catalysis

Catalyst	Elemental analysis (Ni) of as prepared catalyst [wt%]		S_{BET} [$m^2 g^{-1}$]	Particles size [nm] from TEM	
	ICP	SEM EDS		As prepared	After catalysis
10%Ni/CeO_2	9.3	10.8	20	7.6±1.9	12.4±3.3
10%Ni/ZrO_2	10.1	9	15	7.4±1.6	14.9±4.2
10%Ni/$CeZrO_2$	10.7	8.5	71	3.2±0.7	5.9±1.3
10%Ni/TiO_2	7.6	6.9	77	4.6±1	6.2±1.4

The SEM image and SEM-EDS elemental mapping of the as prepared catalysts were given in figure S6,7 (ESI). The SEM-EDS elemental mapping of different region confirms the homogeneous distribution of the nickel all over supports for all the as prepared catalysts. Furthermore, the EDS elemental quantification of the nickel agrees with the elemental analysis data obtained using ICP-AES technique. The BF TEM images of the as prepared supported nickel samples are shown on figure 2. The size and shape of the respective supports remained almost the same after the Ni NPs deposition. The nickel NPs particles size obtained from bright field TEM images are 7.6 ± 1.9, 7.4±1.6, 3.2 ± 0.7, and 4.6 ± 1.0 nm for CeO_2, ZrO_2, $CeZrO_2$ and TiO_2 supports, respectively (table 1). The nickel NPs size distribution histograms were given in figure S8 (ESI). On CeO_2 and ZrO_2, larger NPs and a broader size dispersion were observed (respectively

7.6 ± 1.9 and 7.4 ± 1.6 nm) compared to $CeZrO_2$ and TiO_2 (respectively 3.2 ± 0.7 and 4.6 ± 1.0 nm). The Ni NPs size distribution was largely correlated with the surface area of the materials; supports having higher surface area led to the better dispersion of Ni NPs with relatively small sizes. In order to obtain the structural information of the Ni NPs, HRTEM images were recorded and presented on figure S9 (ESI). The images showed that the nickel crystallinity is poor (amorphous structure) and the corresponding FFT patterns are inconclusive for nickel nanocrystals. The results agree with the powder XRD data which was devoid of any diffraction peaks corresponds to the metallic Ni. Nevertheless, the nickel nanoparticles were found to be uniformly distributed throughout the supports at nanoscale using STEM-EDS elemental mapping (figure S10 and figure 3).

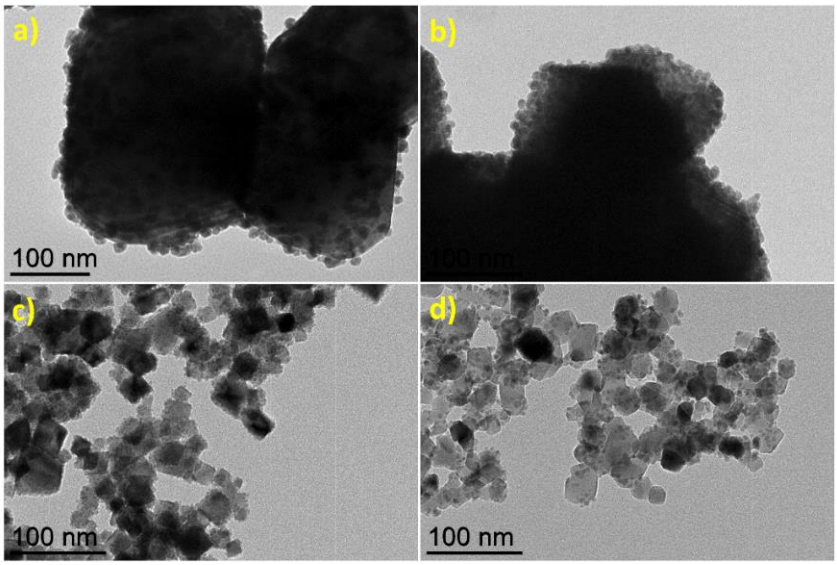

Figure 2. BF TEM images of as prepared, a) 10%Ni/CeO_2, b) 10%Ni/ZrO_2, c) 10%Ni/$CeZrO_2$, and d) 10%Ni/TiO_2.

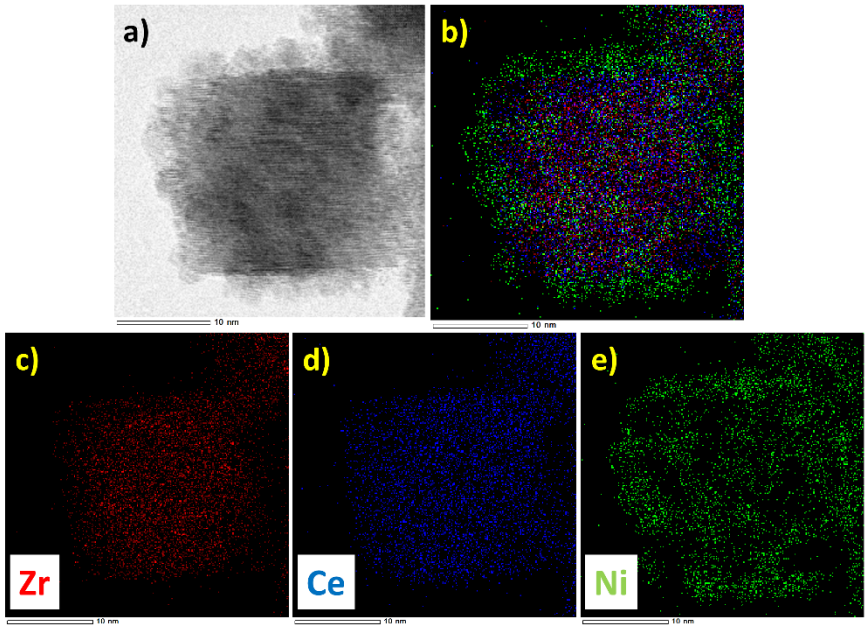

Figure 3. STEM EDS elemental mapping of as prepared 10%Ni/$CeZrO_2$ as a model system, a) BF image, b) overlay of Ni, Ce, and Zr K line maps, c) Zr (red), d) Ce (blue), and e) Ni (green) individual mapping (scale bar: 10 nm).

Magnetic properties of the as prepared catalysts were measured using vibrating sample magnetometry (VSM) and presented in ESI. The saturation magnetization values normalized with respect to the nickel and the coercive fields at 300 and 5 K were tabulated in table S1 and figure S11 (ESI). All the samples except 10%Ni/$CeZrO_2$, showed superparamagnetic behavior at 300 K, whereas at 5 K the NPs exhibit a ferromagnetic behavior. In case of 10%Ni/$CeZrO_2$, the NPs behave like superparamagnetic at both 300 and 5 K. Moreover at 300 K and 5 K, for few of these samples, the magnetization curve at high field of 3 T does not saturate which corresponds to the possible contribution of paramagnetic species present within the system. Herein, the paramagnetic contribution was deduced and the saturation magnetization values were calculated for the

respective samples. The saturation magnetization at 5 K for all the samples were found to be higher than at 300 K. The saturation magnetization (at 5 K) of all the as prepared samples follows the trend, (24.4 emu g_{Ni}^{-1}) 10%Ni/CeO_2 ~ (20.8 emu g_{Ni}^{-1}) 10%Ni/ZrO_2 > (16.4 emu g_{Ni}^{-1}) 10%Ni/TiO_2 > (3.5 emu g_{Ni}^{-1}) 10%Ni/$CeZrO_2$, which is in line with the particles size of the nickel; the larger nickel particles showing higher saturation magnetization than the smaller particles. The saturation magnetization values of all the samples (<25 emu g_{Ni}^{-1}) are significantly lower than the bulk magnetization of nickel (55 emu g_{Ni}^{-1}). This could be probably due to the poor crystallinity of Ni NPs. After cooling down at 5 K and under the applied magnetic field of 3 T, no exchange bias was observed, in agreement with the absence of oxidation (ESI). The coercive field was found to be 30-45 mT for all the samples at 5 K and comparatively higher than 300 K. In the ZFC curve, the presence of a blocking temperature (T_B) indicative of a ferro to paramagnetic transition, was observed respectively at 66 K, 47 K, and 20 K for 10%Ni/CeO_2, 10%Ni/ZrO_2, and 10%Ni/TiO_2 respectively (figure S12, table S1). For 10%Ni/$CeZrO_2$, T_B was found to be below 5 K in agreement with its smallest particle size distribution among all other samples. Further details were given in the ESI. Overall, the magnetic measurement data confirm the other characterization data and demonstrate the presence of metallic nickel nanoparticles presence within the as prepared supported nickel catalysts.

Catalytic performances

The as prepared catalysts were loaded in a glass reactor equipped with a frit and located inside an air-cooled coil delivering an AMF with a frequency of 100 kHz. The composite (catalyst and Fe wool mixture) bed showed good heating efficiency once immersed in the alternating magnetic field (AMF). The temperature ramp rate was high for all catalyst composites (70-100 ˚C min^{-1}) and led to a mean temperature of the composite found between 70 and 350°C according to the coil

power. The temperature response for 10%Ni/TiO_2 catalyst (along with Fe wool) is discussed as a model system (details in the section - "Stability and the effect of dynamic magnetic heating on catalytic activity"). Earlier work from our group (Faure *et. al.*) using Fe powder has emphasized the beneficial role of eddy current generation within the composite bed for producing heat.[20] Herein, the eddy currents flowing through the macroscopic and anisotropic Fe wool under the AMF induces the heating of the catalyst composites. On the other hand, probable very minor contribution of heating of Ni NPs of supported nickel catalysts due to hysteresis loss under the AMF cannot be completely ruled out (Curie temperature of bulk Ni, T_c= 355˚C).[35]

The CO_2 conversion (X_{CO_2}) and CH_4 selectivity (S_{CH_4}) were measured for all the catalysts in the 75 - 350°C temperature range by modulating the applied magnetic field from 1 to 10 mT RMS, at two different GHSV (1500 and 7500 mL g_{cat}^{-1} h^{-1}). Catalytic performances (X_{CO_2} and S_{CH_4}) for all four catalysts with respect to the temperature are outlined on figure 4 and figure S13 (ESI). At low GHSV for all the catalysts, X_{CO_2} increases progressively with increasing temperature and reaches ~95-97% at different reaction temperatures depending on the catalysts with very high S_{CH_4} (>99%). The highest X_{CO_2} values obtained for four different catalysts in terms of reactor temperature (~200˚C) follows the order, 10%Ni/$CeZrO_2$ ~ 10%Ni/TiO_2 > 10%Ni/CeO_2 ~ 10%Ni/ZrO_2. The S_{CH_4} remained >99% at lower temperature (<300˚C), but at >300°C, CO_2 conversion and selectivity towards CH_4 decreased in favor of the reverse water gas shift (RWGS) reaction due to the thermodynamic equilibrium.[3] In the case of 10%Ni/$CeZrO_2$ and 10%Ni/TiO_2, the highest catalytic activity was observed at lower temperature as compared to the other catalysts and these two-catalysts showed up to 60% X_{CO_2} at 150°C, which is a fairly low temperature for CO_2 activation. The temperature measured is the average temperature of the composite bed consisting of Fe wool and supported Ni NPs. It must be pointed out that, in our current set up, and for

comparison purposes, the temperature was measured at the top of the catalyst bed and assumed to be homogeneous throughout the reactor, although this assumption cannot be correct. Thus, it is very challenging to measure the actual surface temperature of catalytically active ferromagnetic metals nanostructures under AMF,[10,30-32] and furthermore, in the heterogeneous catalyst composite we cannot use a simple thermo-couple to measure the mean temperature of the catalytic system. However, considering the previous literature it can be assumed that the actual temperature of the surface of the Ni NPs is probably only slightly underestimated.

At higher GHSV, X_{CO_2} of different catalysts were found to be comparatively lower than at lower GHSV, due to the relative lower residence time of the reactant (figure S13, SI). In the case of 10%Ni/TiO_2, 10%Ni/ZrO_2, and 10%Ni/CeO_2, ~80% X_{CO_2} was observed at 200, 250, and 265˚C, respectively, whereas ~93% of X_{CO_2} was observed for 10%Ni/$CeZrO_2$ at 200˚C. Furthermore, the thermodynamic equilibrium of CO_2 conversion and the corresponding CH_4 selectivity at 1 bar pressure are shown as a comparison scale on figure 4 and figure S13 (ESI).[36] The CO_2 conversion and CH_4 selectivity at different GHSV were found to be close to the thermodynamic limit. The CO_2 methanation activity of the different catalysts was further assessed via calculating the moles of methane obtained at different GHSV and temperatures after normalizing with respect to the total nickel content of the catalyst (table S2, ESI). After normalization ($r_{CH_4}, mol_{CH_4}\ g_{Ni}^{-1}\ h^{-1}$), at low GHSV, the catalysts 10%Ni/$CeZrO_2$ and 10%Ni/TiO_2 proved to be the most active at 200°C whereas the r_{CH_4} values (~0.12-0.17 $mol_{CH_4}\ g_{Ni}^{-1}\ h^{-1}$) were almost similar for all the four catalysts at 250°C (X_{CO_2}>90% and S_{CH_4}>99%). At higher GHSV and at 200 and 250˚C, the normalized rate follows the same order, which is, 10%Ni/TiO_2> 10%Ni/$CeZrO_2$> 10%Ni/ZrO_2> 10%Ni/CeO_2. It is quite hard to compare the reaction rates/performances obtained in this process with those of traditional state-of-the-art heterogeneous catalytic processes, due to a large difference in the

reactor setup, operation condition, catalyst synthesis, etc. Considering the previous literature report on AMF induced methanation reaction, at low to mid temperature range (200-250˚C), the catalytic reactivity and the normalized methane production rate of 10%Ni/TiO_2 and 10%Ni/$CeZrO_2$ were found to be quite high (0.58-0.68 $mol_{CH_4}\ g_{Ni}^{-1}\ h^{-1}$) at 7500 mL g_{cat}^{-1} h^{-1} GHSV.[31] We believe that the current process and the methane production rate could be further improved with the newly designed reactor in our lab which can operate at higher flow rates (or GHSV). Although considering the low temperature catalytic activity of these supported catalysts, it can be stated that methanation under AMF clearly outperforms conventional heating mediated processes reported for similar supported catalysts, because of a better heat management of AMF induced processes (kinetically limited process rather than the heat transfers limited process).[18,31]

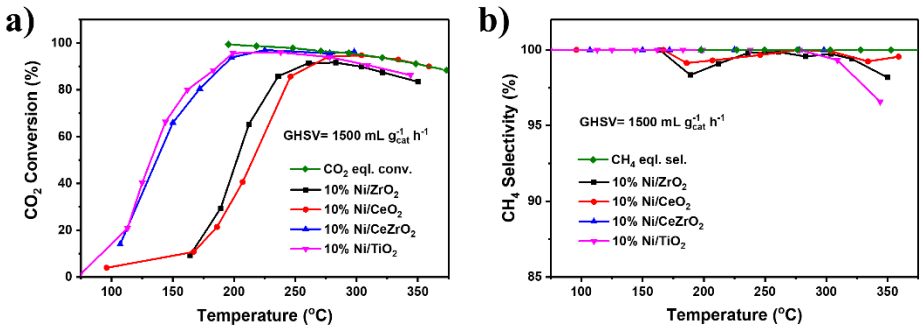

Figure 4. Catalytic activity of 10%Ni/CeO_2, 10%Ni/ZrO_2, 10%Ni/$CeZrO_2$, and 10%Ni/TiO_2 at GHSV = 1500 mL g_{cat}^{-1} h^{-1}, a) %CO_2 conversion (X_{CO_2}) vs. temperature, and b) %CH_4 selectivity (S_{CH_4}) vs. temperature plots. The thermodynamic equilibrium CO_2 conversion and CH_4 selectivity at 1 bar pressure is shown as a green line in both graphs.[36]

The higher catalytic activity for 10%Ni/TiO_2 and 10%Ni/$CeZrO_2$ as compared to the 10%Ni/CeO_2 and 10%Ni/ZrO_2 at lower reaction temperature could be rationalized in terms of the

better dispersion of the nickel NPs, lower NPs size, and high surface area for 10%Ni/TiO_2 and 10%Ni/$CeZrO_2$ catalysts. Each catalyst was further characterized using powder XRD, BF TEM, VSM, and XPS techniques after 14 hours of catalytic test under different temperatures and flow rates. Powder XRD patterns were compared for both as-prepared and spent catalysts for each supported nickel catalysts and are given in figures S15 (ESI). In case of the as-prepared catalysts, due to the small crystallite size of the Ni NPs, Ni(0) diffraction peaks were absent. However, in case of the spent catalysts, additional diffraction peaks for fcc Ni(0) were observed, because of the nanoparticles sintering and crystallization of the Ni NPs during catalysis experiments. Also, in the same pattern and at a similar 2-theta value, bcc (body-centered cubic) Fe(0) could be identified and attributed to the leaching of Fe wool particles while recovering the post-catalytic sample. The presence of both Ni(0) and Fe(0) were confirmed for spent 10%Ni/TiO_2 catalysts as a model system through Rietveld refinement (figure S16, ESI). Hence, the crystallite size calculation from the XRD patterns could not be carried out for the spent catalysts.

In order to further evaluate the extent of sintering of Ni NPs during the catalytic test, BF TEM analysis was performed for all the spent catalysts. BF TEM images and the respective histograms of the Ni NPs size distribution for the spent catalyst are presented on figure 5 and figure S17 (ESI), respectively. Table 1 shows the Ni NPs size before and after catalysis. Qualitatively, the size and shape of the support crystals in case of spent catalysts remain unchanged after the catalysis with respect to the as prepared catalysts. The calculated Ni NPs size for the CeO_2, ZrO_2, $CeZrO_2$, and TiO_2 supported samples are 12.4 ± 3.3, 14.9 ± 4.2 nm, 5.9 ± 1.3 and 6.2 ± 1.4, respectively. The relative extent of sintering of Ni NPs in the spent catalysts for $CeZrO_2$ and TiO_2 supported samples was found to be lower as compared to the ZrO_2 and CeO_2. Despite the presence of a relatively smaller size of Ni NPs in the case of the TiO_2 and $CeZrO_2$ supports, moderate increase in the Ni

NPs size in the case of the TiO_2 and $CeZrO_2$ supports, as compared to the CeO_2 and ZrO_2 supports, further indicates the reduced surface mobility of the Ni NPs and their higher degree of dispersion on $CeZrO_2$ and TiO_2 supports. The STEM-EDS elemental mapping further shows that in spite of the sintering of Ni NPs, the distribution of the NPs is still uniform and less aggregated. The STEM-EDS elemental mapping of 10%Ni/$CeZrO_2$, and 10%Ni/TiO_2 are shown in figure S18 (ESI). Overall, these experiments show that the system does not undergo any critical evolution during the magnetically heated catalysis.

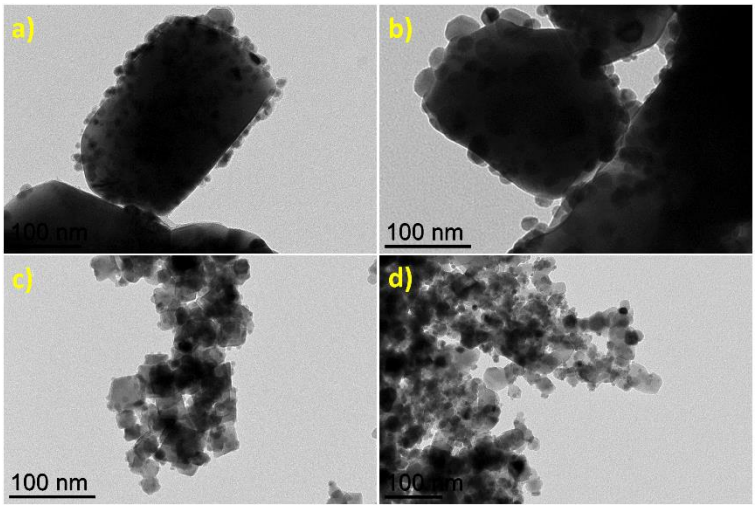

Figure 5. BF TEM images of spent catalyst, a) 10%Ni/CeO_2, b) 10%Ni/ZrO_2, c) 10%Ni/$CeZrO_2$, and d) 10%Ni/TiO_2.

The sintering of Ni NPs during the catalysis was further investigated through measurements of the magnetic properties of the spent catalysts. The hysteresis curves for spent catalysts at 300 and 5 K are shown on figure S19 (ESI). The saturation magnetization and coercive field values are given in table S3 (ESI). Due to some extent to the slight increase in particles size and more

important to the improved crystallinity of Ni NPs, the saturation magnetization of the Ni improved largely as compared to their parent analogues and approaches the bulk saturation magnetization of nickel (55 emu g_{Ni}^{-1}). Slightly higher saturation magnetization of the spent catalysts than the bulk nickel could be rationalized to the presence of small Fe wool impurities in the samples, which was further supported by the powder XRD data. In case of the spent catalysts, no exchange bias was observed at 5 K under 3 T applied magnetic field, further confirming the absence of oxidation. Magnetic properties measurement data analyses are discussed in the ESI.

In order to evaluate the electronic effects of the supports on nickel and the possible origin of the differences in catalytic activity, Ni 2p core level XPS spectra were measured for 10%Ni/CeO_2, 10%Ni/ZrO_2, 10%Ni/$CeZrO_2$, and 10%Ni/TiO_2, before and after catalysis. The stacked plot of Ni $2p_{3/2}$ core level spectra of as prepared and spent catalysts for each supported nickel sample is given in figure S21 and S31 (ESI). The qualitative analysis of XPS spectra from peak maxima demonstrate the presence of Ni^0 and oxidized Ni^{2+} species at the surfaces of all fresh and spent catalysts. Partial oxidation of the catalysts could not be prevented due to air exposure of all samples during the transfer to the instrument. The qualitative analysis of binding energies of the $2p_{3/2}$ metallic Ni peak for different as prepared catalysts are in the range of 852.4-852.5 eV. The binding energies corresponding to metallic Ni in the spent catalysts were found to be slightly lower (852.2-852.1 eV) than in the as prepared catalysts. Very slight variations of binding energies of Ni^0 were indeed observed by changing the substrate before catalysis, and almost no variation was observed after catalysis. As such differences of ~0.1-0.2 eV was in the margin of error of the measurements, it was difficult to deduce any significant information from this study. In any case, effects of metal-support interaction on the electronic density of Ni^0, if they exist, are extremely weak, and less important than the reductive treatment effect associated to the catalytic conditions. All these results

and characterizations of post catalysis samples indicate that, the different reducible supports used in this work have a strong influence on the deposited nickel particles size, and dispersion, which probably dictate the catalytic activity and the methane selectivity at different extents. Moreover, these results are quite encouraging for further investigating in detail the performances of these catalysts and for evaluating their performances for other catalytic transformations.

Energy efficiency of the process

An important criterion to be considered when considering the possibility to develop catalysis using magnetic induction is the overall energy efficiency of the process. High energy costs would definitively prevent this technology to be implemented in P2G process, and therefore efforts have been made to evaluate and improve the energy efficiency of the process reported herein.[33] There are very few reports to the best our knowledge which have discussed the energy efficiency of a catalytic process under magnetic induction mediated heating.[20,34] Recently, Almind *et al.* has discussed the optimization of the coil geometries and its influence on the energy efficiency of the induction-heated methane steam reforming reaction.[34] The ability of our process to store energy was assessed using a typical efficiency ratio, considering the output power, carried by the CH_4 flow, divided by the input power, carried by H_2 flow and the power required for the coil (equation 1).[33]

$$\eta = \frac{P\ (CH_4)}{P(H_2) + P_{Coil}} \times 100 \qquad equation\ (1)$$

In this definition, the power carried by gases is the power that would be generated by the combustion of that gas flow (equation 2), or:

$$P(X) = \dot{m}(X) \times HHV(X) \qquad equation\ (2)$$

where, $\dot{m}(X)$ is the mass flow rate of the gas (mg s^{-1}) and HHV(X) is the highest heating value (J mg^{-1}) of the gas. Because of the high intrinsic heating values of CH_4 and H_2, and in the ideal case where P_{Coil} is 0 W, the energy efficiency ratio is capped at 83% as seen on figure 6. Also, the figure 6 clearly shows that getting close to that top can be achieved by 1) decreasing P_{Coil}, especially at low flow rates, and 2) overall increasing the CH_4 out flow rate.

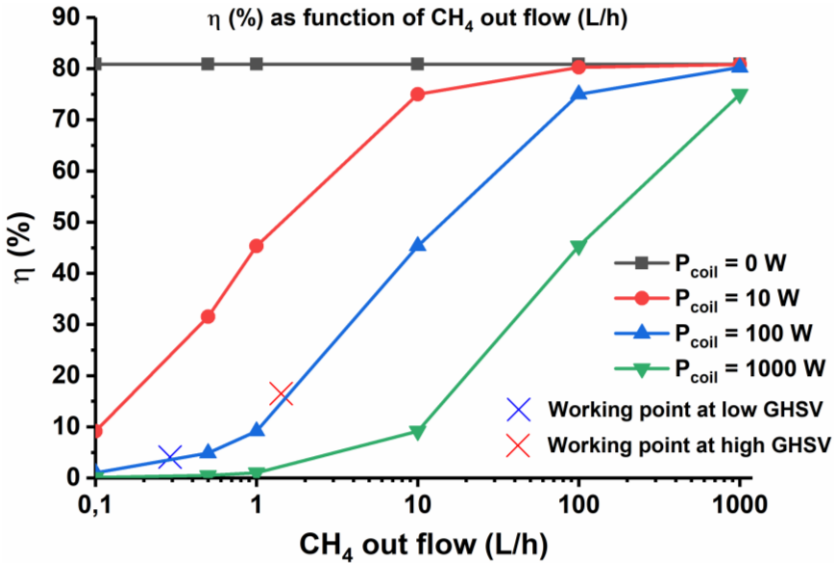

Figure 6. Energy efficiency of the process plotted against methane outflow rate at different background power of the coil.

In this study, the magnetic field needed for CO_2 methanation was < 12 mT RMS which requires for the coil a minimum working power P_{Coil} = 70 W. In the ideal case scenario, at 125 mL min^{-1} flow (GHSV=7500 mL g_{cat}^{-1} h^{-1}) and Y_{CH_4} = 100%, and considering the necessary P_{Coil} value, the energy efficiency (η) cannot exceed 17.4%. Therefore, we will consider that this is the maximum value reachable for our present set-up. Figure 7 depicts the energy efficiency obtained for 10%Ni/CeO_2, 10%Ni/ZrO_2, 10%Ni/$CeZrO_2$, and 10%Ni/TiO_2 catalyst, at both high and low

GHSV, as a function of the magnetic field applied. Because all the catalysts are operative in the same range of magnetic field, the energy efficiency is mainly dominated by the CH_4 yield, and therefore, the most active catalysts also appear to be the most energy efficient. For all the catalysts, the energy efficiency at low GHSV (1500 mL g_{cat}^{-1} h^{-1}) reaches the laboratory set up limit (~4%). On the other hand, 10%Ni/$CeZrO_2$ was the most efficient catalyst at high GHSV (7500 mL g_{cat}^{-1} h^{-1}), reaching η = 16.2% for the process (shown as red working point on figure 6). Moreover, the experimental values illustrate well that a higher flow will yield a higher energy efficiency ratio if P_{Coil} can be kept in the same of order of magnitude, since at low GHSV (1500 mL g_{cat}^{-1} h^{-1}), η was $\leq$ 4% (shown as blue working point on figure 6). Overall, the reported catalysts work quite efficiently at low to mid temperature (200-300°C) range with high energy efficiency at two different GHSV.

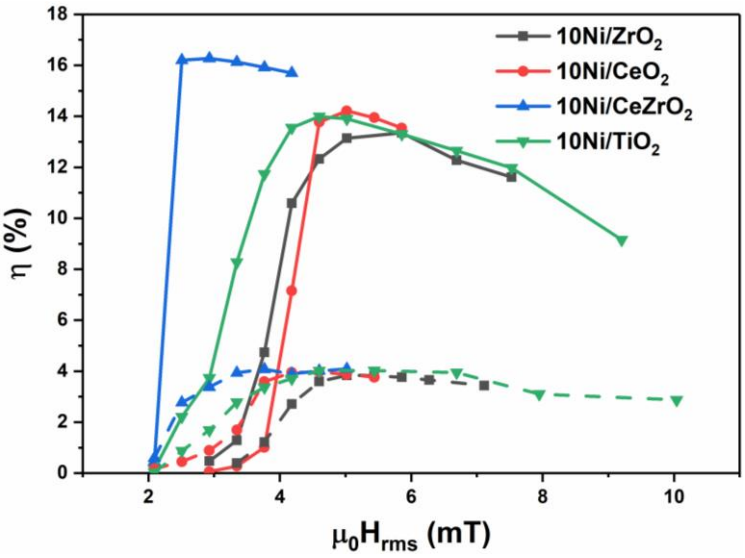

Figure 7. Energy efficiency of the Sabatier reaction for 10%Ni/CeO_2 (red), 10%Ni/ZrO_2 (grey), 10%Ni/$CeZrO_2$ (blue), and 10%Ni/TiO_2 (green) catalysts at two different GHSV (1500 and 7500 mL g_{cat}^{-1} h^{-1}) plotted with respect to the applied magnetic field. The solid lines represent the energy

efficiency at 7500 mL g_{cat}^{-1} h^{-1} GHSV and the dashed lines correspond to the values obtained at 1500 mL g_{cat}^{-1} h^{-1} GHSV.

In a previous report by Faure *et.al.*, the maximum energy efficiency of ~4% at low flow (25 mL.min^{-1}) had been reached.[20] In the present study, the 17% energy efficiency at 125 mL min^{-1} flow that was predicted was nearly reached. In that previous study, the catalytic bed was made of 10%Ni/CeO_2 as a catalyst, commercial iron powder as a heating agent and SiC particles as a spacer. The improvement herein observed is mainly due to, 1) the use Fe wool, a better heating agent SAR-wise, allowing the use of a lower magnetic field and low operational power for the coil, 2) the use of a more active catalyst, namely 10%Ni/$CeZrO_2$, enabling high conversion rate at higher GHSV. The maximum energy efficiency calculated for the other catalysts at high GHSV, namely 10%Ni/CeO_2, 10%Ni/ZrO_2, and 10%Ni/TiO_2 was slightly less (~ 14% as compared to the 16.2% for 10%Ni/$CeZrO_2$). However, considering the cost, catalytic activity, and the availability of the supports, TiO_2 supported catalyst (10%Ni/TiO_2) was chosen as a model system and modifications of the catalysts were carried out to achieve a higher energy efficiency at high flow/GHSV (125 mL min^{-1}/7500 mL g_{cat}^{-1} h^{-1}).

Modification of 10%Ni/TiO_2 and its catalytic performance

With the aim of exploring the effect of the synthetic method on the catalytic activity, 10 wt% nickel supported on TiO_2 was synthesized by the conventional impregnation method. The onset of the reduction of calcined 10%Ni/TiO_2_CI was investigated using *in-situ* XRD technique and found that 300 ˚C is enough to initiate the reduction of nickel oxide to nickel (details in ESI). The as prepared calcined sample was characterized using XRD, SEM and SEM-EDS elemental mapping,

BF TEM, XPS, and ICP-AES techniques, and the spent catalyst (after reduction followed by catalysis) was characterized by XRD, BF TEM, STEM EDS elemental mapping, and XPS techniques. The characterization details and discussion are given in the ESI. The as prepared samples morphology and structural characterization refers to the structure consist of TiO_2 supported homogeneously dispersed NiO NPs.

It has been reported that both Ru and Ni supported on TiO_2 are the efficient catalysts for Sabatier reaction[22-29] and that a small amount of Ru doping could alter the CO_2 methanation activity and the CO/CH_4 selectivity of Ni/TiO_2. In order to investigate the effect of Ru doping on Ni/TiO_2 in catalytic activity and overall energy efficiency of the process, $10\%RuNi/TiO_2$ was synthesized via sequential decomposition of Ni and Ru precursors and was tested for Sabatier reaction. The elemental composition was measured to be ~9.5% Ni and 0.5% Ru, via ICP-AES and SEM-EDS methods (table 2). The as prepared $10\%RuNi/TiO_2$ was characterized using XRD, SEM and SEM-EDS elemental mapping, BF TEM, STEM EDS elemental mapping, and XPS techniques (details structural characterization data discussed in the ESI). The structural and morphological characterization of $10\%RuNi/TiO_2$ showed that both Ni and Ru are homogeneously distributed over TiO_2 and the overall structure matches well with the pure nickel analogue $10\%Ni/TiO_2$.

Table 2. Elemental and particles size analysis data of 10%Ni/TiO_2, 10%RuNi/TiO_2 and 10%Ni/TiO_2_CI

Catalyst	Elemental analysis (Ni) for as prepared samples		Particles size [nm] from TEM	
	ICP [wt%]	SEM EDS [wt%]	As prepared	After catalysis
10%Ni/TiO_2	7.6	6.9	4.6±1	6.2±1.4
10%Ni/TiO_2_CI	9.6	9.7	-	-
10%RuNi/TiO_2	9.6; (Ru - 0.5)	7.5; (Ru – 0.6)	4.7 ± 1.1	5.6 ± 1.4

The catalytic activity of the 10%RuNi/TiO_2 and 10%Ni/TiO_2_CI for Sabatier reaction was investigated at two different gas flow (25 and 125 mL min^{-1}) and compared with the 10%Ni/TiO_2 for a same amount of catalyst mass loading (figure 8a, figure S30 in the ESI). The characterizations of the spent 10%RuNi/TiO_2 and 10%Ni/TiO_2_CI catalysts are discussed in the ESI. It was found that at 25 mL min^{-1} gas flow (GHSV=1500 mL g_{cat}^{-1} h^{-1}), both 10%Ni/TiO_2 and 10%Ni/TiO_2_CI exhibit similar temperature vs X_{CO_2} profiles, whereas 10%RuNi/TiO_2 needed a slightly higher temperature (~255˚C) to achieve the yields and selectivity's of 10%Ni/TiO_2 (~96% X_{CO_2} and >99% S_{CH_4} achieved at ~200˚C) (figure S30a, ESI). Interestingly at 125 mL min^{-1} gas flow (GHSV=7500 mL g_{cat}^{-1} h^{-1}), the 10%Ni/TiO_2 and 10%Ni/TiO_2_CI samples showed similar temperature vs X_{CO_2} profile with maximum conversion of ~81% (~99% S_{CH_4} at 210˚C), however 10%RuNi/TiO_2 needed slightly higher temperature (250˚C) to achieve even higher conversion ~92% (X_{CO_2}) with >99% S_{CH_4}. Although at high GHSV with increasing temperature, the S_{CH_4}dropped for all the samples and follow the order, 10%Ni/TiO_2 <10%Ni/TiO_2_CI <10%RuNi/TiO_2 (at 350°C). The Ru

doping to Ni/TiO_2, not only increases the catalytic activity (X_{CO_2}), but also increases the S_{CH_4} and the 10%RuNi/TiO_2 sample exhibit 88% X_{CO_2} with >99% S_{CH_4} at 350˚C.

The normalized methane production rate at high GHSV and at 200˚C follows the order, 10%Ni/TiO_2 >10%Ni/TiO_2_CI ~10%RuNi/TiO_2, whereas upon increasing the temperature to 250˚C, the X_{CO_2} and S_{CH_4} for 10%RuNi/TiO_2 increases and the normalized methane production rate (0.64 $mol_{CH_4}\ g_{Ni}^{-1}\ h^{-1}$) becomes comparable with the 10%Ni/TiO_2 (0.68 $mol_{CH_4}\ g_{Ni}^{-1}\ h^{-1}$). At this point, it is worth mentioning that, the S_{CH_4} was >99% for 10%RuNi/TiO_2 as compared to the ~97% for 10%Ni/TiO_2 at 250˚C. The X_{CO_2} and temperature of the system with respect to the applied magnetic field is shown in figure S30b (ESI). At low GHSV, the energy efficiency for all the three samples is close to the theoretical limit (~4%). At high GHSV, 10%RuNi/TiO_2 at is the most energy efficient catalyst (figure 8b). In order to further improve the process, we are currently investigating the semi-industrial upgrade of our apparatus to be able to work at much higher reactant flow rates.

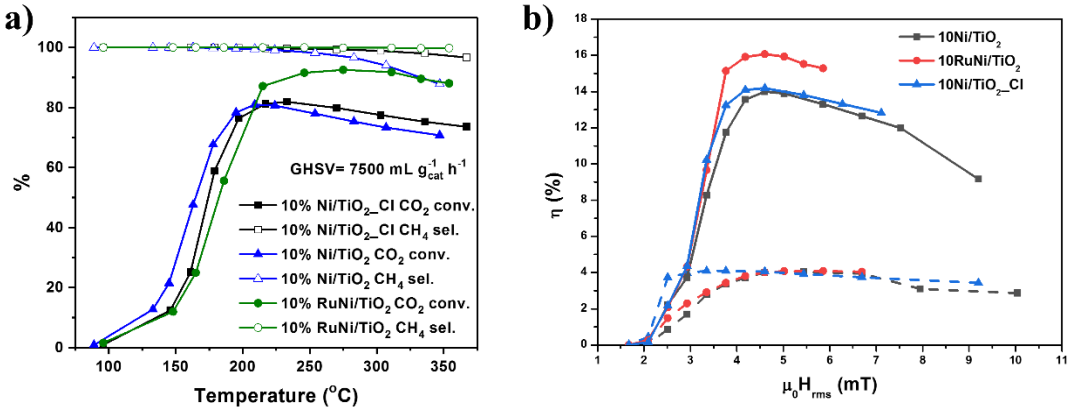

Figure 8. a) Catalytic conversion of CO_2 vs. temperature plot for 10%Ni/TiO_2, 10%Ni/TiO_2_CI, and 10%RuNi/TiO_2 (left hand Y-axis: %CO_2 conversion X_{CO_2} and %CH_4 selectivity S_{CH_4}) at GHSV = 7500 mL g_{cat}^{-1} h^{-1}, and b) energy efficiency of the Sabatier reaction for 10%Ni/TiO_2

(grey), 10%RuNi/TiO_2 (red), and 10%Ni/TiO_2_CI (blue) catalyst at two different GHSV (1500 and 7500 mL g_{cat}^{-1} h^{-1}) plotted with respect to the applied magnetic field. The solid and dashed line correspond to the energy efficiency values obtained at 7500 and 1500 mL g_{cat}^{-1} h^{-1} GHSV, respectively.

Stability and the effect of dynamic magnetic heating on catalytic activity

The key perk of magnetic heating being its dynamic behavior, and in order to model intermittency, a catalytic test was performed with the coil alternating between on and off power during a 7 h run. The catalytic test was performed at 7500 mL g_{cat}^{-1} h^{-1} GHSV using 10%Ni/TiO_2 as the catalyst. Figure 9 shows the catalytic behavior of 10%Ni/TiO_2 and the reactor temperature profile under random coil power on/off condition. As soon as the coil turned on, the temperature reached approx. 200°C in 2 min and within 15-20 min of reaction, X_{CO_2} reached its usual value of approx. 80%. Similarly, when the coil was turned off, the reactor returned to room temperature (~30˚C) in the course of approx. 2-3 min and the resulting X_{CO_2} value dropped below 10%. Although, the selectivity towards CH_4 remained at >99%. Over 8 random on/off cycles, the ~80% X_{CO_2} value could always be reached repeatedly. This particular experiment further demonstrates the applicability of the Sabatier process under magnetic induction mediated heating towards intermittency.

10.1002/cssc.202201724

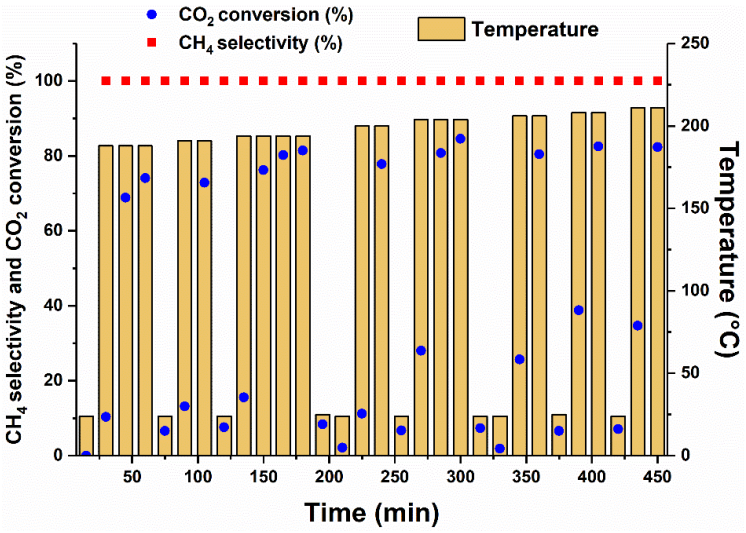

Figure 9. X_{CO_2} and S_{CH_4} (left hand Y-axis) and temperature (right hand Y-axis) as a function of time. Catalyst is 10%Ni/TiO_2. Throughout the experiment, the applied magnetic field value was kept constant while the coil was turned on.

The catalytic stability test was performed for 10%Ni/TiO_2 catalyst at ~220˚C and 7500 mL g_{cat}^{-1} h^{-1} GHSV (1:4 CO_2 to H_2 v/v ratio) for 45 h on stream. Figure 10 shows the stability test result for 10%Ni/TiO_2 catalyst. It was found that the X_{CO_2} and S_{CH_4} values remain stable over the 45 hours' time period. The catalytic stability test for the 10Ni/TiO_2 along with iron wool also demonstrates the robustness of the concept towards large scale implementation of Sabatier process under magnetic heating condition.

10.1002/cssc.202201724

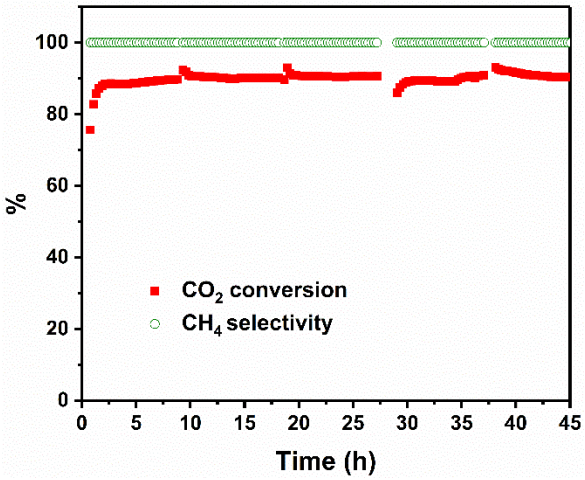

Figure 10. Catalytic stability test of 10%Ni/TiO_2 at GHSV = 7500 mL g_{cat}^{-1} h^{-1} (H_2 flow = 100ml min^{-1}, and CO_2 flow = 25 mL min^{-1}) and at ~220˚C, X_{CO_2} and S_{CH_4} (left hand Y-axis) plotted as a function of time on stream. The small fluctuation in the stability test data arises from the switching of gases.

Conclusions

In this work, we describe the design of a catalytic system for CO_2 methanation adapted to magnetic heating. The heating agent used is a cheap commercial iron wool heated by Eddy currents. The catalyst consists of 10% Ni prepared by an organometallic approach and deposited on four different oxides (TiO_2, CeO_2, ZrO_2, $CeZrO_2$). In the case of the TiO_2 support, the performances of the Ni catalyst were compared with those of an analogous 10% Ni catalyst prepared by a classical impregnation/reduction method and with those of a $Ru_{0.5}Ni_{9.5}$ catalyst. All catalysts were thoroughly characterized before and after catalysis by state-of-the-art methods. In all cases, the system proved to be very selective for methane production at low working temperatures and reached excellent CO_2 conversion values (up to ~90% at 7500 mL g_{cat}^{-1} h^{-1} GSHV). Furthermore,

stop and go experiments demonstrated the adaptation of this system to intermittency. Finally, the energy efficiency of the catalyst could approach the theoretical limit of our lab-scale set-up. We are now transposing this system to a pilot scale where the theoretical limit of energy efficiency is much higher and which should allow evaluating the interest in this process at the industrial scale.

Experimental section

Materials

Mesitylene (99.0%), tetrahydrofuran (99.9%), and toluene (>99.0%) were purchased from VWR, Carlo Erba, and Fischer Scientific, respectively. The solvents were dried on an alumina-desiccant solvent purifier and degassed by Argon (Ar) bubbling for 20 minutes before storing in the glove box. Bis(1,5-cyclooctadiene)nickel(0) ($Ni(COD)_2$, 98%) and (1,5-Cyclooctadiene)(1,3,5-cyclooctatriene)ruthenium (Ru(COD)(COT)) were obtained from Strem and Nanomeps, respectively, and used without further purification. Cerium dioxide (CeO_2, 99.9%), zirconium dioxide (ZrO_2, 99.0%), cerium zirconium mixed oxide ($CeZrO_2$, 99.0%), and nickel nitrate ($Ni(NO_3)_2.6H_2O$, >98%) were purchased from Sigma-Aldrich. Titanium dioxide (P25 TiO_2, >98.0%) was obtained from Acros Organics. All supports were dried in a pre-heated oven at 100˚C for overnight before being introduced in the glove box. Fe wool (commercial branding “Paille de fer FINE”) was purchased from Gerlon and used without further purification. The commercial supports and the Fe wool characterizations are available in the supporting information (ESI, figure S1-3). All gases were supplied by Air-Liquide. Purity of the gases are: CO_2 Alphagaz N48 (≥ 99.998 %), H_2 N55 (≥ 99.9995 %), and Ar N56 (>99.9996 %).

Synthesis of supported Ni NPs

Synthesis of supported Ni NPs via Organometallic decomposition route

The supported Ni NPs (10 wt%) were prepared by thermal decomposition of $Ni(COD)_2$ precursor in presence of the support and inspired by the previous literature report.[20] All the organometallic decomposition manipulation step was carried out in a Fisher-Porter (FP) bottle. In a typical procedure, support (2.5 g) was added to a yellow-solution of $Ni(COD)_2$ (1.301 g, containing 0.278 g Ni) in mesitylene (30 mL) in the glove box. The reaction mixture was vigorously stirred for 1 h at room temperature, and then introduced in a 150°C pre-heated oil bath for 1 h, with vigorous stirring under Ar atmosphere. The black powder obtained was collected by decantation, and washed with 4×10 mL of toluene. Finally, the powder was dried under vacuum for 6 h and stored inside the glove box.

Synthesis of Titania supported Ni NPs via impregnation method

The catalysts have been first prepared from organometallic precursors which, in turn, were prepared and handled using mesitylene, toluene and THF as solvents. However, after having identified the best catalyst, we turned to an alternative classical synthesis which uses water as a solvent. Also, TiO_2 supported Ni NPs with 10 wt% metal loading was prepared by conventional impregnation method. Typically, 5 g of TiO_2 was added to an aqueous solution of nickel nitrate (2.572 g, 8 mL) and the solution was stirred for 3 h. After that, the resultant slurry was dried at 110˚C for 12 h, followed by calcination under air at 300˚C for 3 h. The sample is named as 10%Ni/TiO_2_CI. Finally, the sample was reduced in-situ in the reactor under magnetic induction mediated heating. Typically, 0.8 g of Fe wool and 1 g of 10%Ni/TiO_2_CI was loaded together in a glass reactor (detailed information about the catalytic reactor and catalytic reaction setup was

given in the catalytic test section) and the temperature was raised to 300˚C and hold for 2 h under 30 mL min^{-1} of pure H_2 flow. It has been observed that during the reduction process, the reactor temperature increased from 300 to 314˚C. The increase of temperature could be due to the contribution of additional heat generated by exothermic reduction process of nickel oxide to nickel. Followed by the reduction of nickel oxide, the reactor temperature decreased to 80˚C and the gas flow was changed from pure H_2 to a mixture of H_2 and CO_2 and subsequently, the catalytic reaction was started.

Synthesis of Titania supported RuNi NPs via Organometallic decomposition route

TiO_2 supported Ni@Ru NPs (10 wt% total metal content) were prepared by decomposition of $Ni(COD)_2$ followed by the decomposition of Ru(COD)(COT) in presence of TiO_2 support. In a typical procedure, TiO_2 (1.34 g) was added to a yellow-solution of $Ni(COD)_2$ (0.694 g, 9.5 wt% Ni) in mesitylene (25 mL) in the glove box. The obtained solution was vigorously stirred for 1 h at 30˚C, and then introduced in a 150°C pre-heated oil bath for 1 h, with stirring under Ar atmosphere. The black powder obtained was separated by decantation, and washed 3 times with 5 mL of THF. After the last washing, 10 mL of THF was added and the FP bottle was charged with 3 bars of H_2 and stirred for 2 h at 30˚C. 1 bar of pressure drop was noted during this period. Subsequently, the residual H_2 was vented inside the glove box, and the solution is stirred for additional 5 min to remove the dissolved H_2. Subsequently, Ru(COD)(COT) (0.027 g, 0.5 wt% Ru) was introduced in the reaction mixture and the resulting solution was stirred for 2 h at 30˚C. Finally, the solution was exposed to 3 bars of H_2 for 4 h. The black powder obtained was separated by decantation, and washed with 3×5 mL of THF. After washing, the powder was dried under vacuum for 6 h. The sample is abbreviated as 10%RuNi/TiO_2.

Characterization of the catalysts

Powder X-ray diffraction (XRD) patterns were recorded using a PANalytical Empyrean diffractometer (Co source, Kα - 1.79 Å). In-situ XRD experiment was performed for 10%Ni/TiO_2_CI sample and the experimental details were given in the ESI. Scanning electron microscopy (SEM) imaging was carried out using a JEOL JSM-7800F microscope with field emission gun (FEG) source. SEM-EDS elemental mapping was carried out with an EDS Bruker XFlash detector attached to the microscope. Bright field transmission electron microscopy (BF TEM) imaging was carried out for obtaining the histogram of nickel NPs dispersed in different supports using a JEOL JEM 1400 TEM microscope equipped with a tungsten filament and the operating voltage was 120 kV. For each sample, 150 particles were measured on the ImageJ software for plotting the histogram. High resolution transmission electron microscopy (HRTEM) images were acquired using a probe Cs corrector and cold FEG gun equipped JEM-ARM200F microscope. The resolution of the microscope is: TEM imaging resolution = 1.9 Å point, and 1.0 Å line, and STEM imaging resolution = 0.78 Å (STEM HAADF 200kV). The camera used for the imaging was GATAN ULTRASCAN 2k × 2k Model 994. STEM-EDS elemental mapping was carried out using a high angle SDD CENTURIO-X (resolution 129 eV) detector attached to the TEM. The operating voltage of the microscope was 200 kV. The equipment is installed in the R. Castaing micro-characterization platform in Toulouse. Nitrogen physisorption isotherms were obtained using an Autosorb iQ (Model 6) instrument from Quantachrome. Specific surface area was calculated using Brunauer–Emmett–Teller (BET) method. The samples were degassed at 200˚C for 4 h prior to the measurement. Elemental analysis of nickel was performed via Inductively Coupled Plasma - Atomic Emission Spectroscopy (ICP-AES) method using an iCAP 6300 ICP Duo Spectrometer. ICP-AES measurements were carried out at the Laboratoire de

Chimie de Coordination (LCC) in Toulouse. The photoelectron emission spectra were recorded using a monochromatized Al-Kα (hν = 1486.6 eV) source on a ThermoScientific K-Alpha system. The X-ray Spot size was about 400 µm. The Pass energy was fixed at 30 eV with a step of 0.1 eV for core levels and 160 eV for surveys (step 1eV). The spectrometer energy calibration was done using the Au $4f_{7/2}$ (83.9 ± 0.1 eV) and Cu $2p_{3/2}$ (932.8 ± 0.1 eV) photoelectron lines. XPS spectra were recorded in direct mode N (Ec) and the background signal was removed using the Shirley method. The flood Gun was used to neutralize charge effects on the top surface. Each spectrum was calibrated using the C1s (284.6 ± 0.1 eV) peak position. The error in the measurements are ±0.1 eV. The magnetic properties of the samples were measured using a vibrating scanning magnetometer (VSM, in the physical property measurement system (PPMS Evercool II) from Quantum Design). The magnetization versus magnetic field measurements (hysteresis loop) at 300 and 5 K were carried out up to ±3T external field. The temperature dependent magnetic susceptibility at zero-field-cooled (ZFC) and field-cooled (FC) conditions were measured at 5 mT field in the 5 - 300 K range. For the magnetic measurements dry powder samples were loaded in a capsule inside the glovebox.

Catalytic tests

The catalytic tests were carried out in a borosilicate glass reactor (d_{int} = 1 cm, L = 18 cm) with porous silica bed fused at the middle. The reactor was placed in an air-cooled coil delivering an alternating magnetic field (AMF) oscillating at a frequency of 100 kHz with an amplitude between 0 and 42 mT RMS provided by Induction Partners. For this study, the applied magnetic field was kept < 12 mT RMS, and the coil's power required was P_{coil} = 70W. The reactor was equipped with a glass capillary at the top, allowing to measure the temperature at the surface of the catalytic bed with K-type temperature probe. The gas configuration was down-flow, and a round bottom flask

at the bottom of the reactor was placed to collect the water (a side product of the reaction). A typical catalytic testing setup figure was given in the figure S4 (ESI).

The outlet gases were analyzed by gas chromatography (PerkinElmer 580) equipped with both a Thermal Conductivity Detector (TCD) and a Mass Spectrometer (PerkinElmer Clarus SQ8T). CO_2 conversion (X_{CO_2}), selectivity towards CH_4 (S_{CH_4}), and CH_4 yield (Y_{CH_4}) were calculated using a relative ratio of chromatogram areas of the carbon-based reactants and products, as described in equations 3-5. The response factors (RF_{gas}) of each gas for the thermal conductivity detector were assessed by injecting a known concentration of these gases in the TCD.

$$X_{CO_2} = \left(\frac{A_{CH_4} \times RF_{CH_4} + A_{CO} \times RF_{CO}}{A_{CO_2} \times RF_{CO_2} + A_{CH_4} \times RF_{CH_4} + A_{CO} \times RF_{CO}} \right) \times 100 \qquad equation\ (3)$$

$$S_{CH_4} = \left(\frac{A_{CH_4} \times RF_{CH_4}}{A_{CH_4} \times RF_{CH_4} + A_{CO} \times RF_{CO}} \right) \times 100 \qquad equation\ (4)$$

$$Y_{CH_4} = \left(S_{CH_4} \times X_{CO_2} \right) \times 100 \qquad equation\ (5)$$

For a catalytic test, 1 g of catalyst and 0.8 g of Fe wool (heating-agent) were loaded together in the reactor. Experiments were carried out at two different gas flow namely, 25 and 125 mL min^{-1} (H_2/CO_2 ratio of 4/1, v/v), corresponding respectively to GHSVs of 1500 and 7500 mL g_{cat}^{-1} h^{-1}. The Fe wool mass was not considered in GHSV, since Fe wool catalytic activity was tested as negligible. Temperature (75 to 360°C) was adjusted through modulating the applied magnetic field from 1 to 12 mT RMS. Steady state was considered to be reached within 30 minutes at each temperature tested.

For the catalytic stability test, 1 g of 10Ni/TiO_2 and 0.8 of iron wool were loaded together in the reactor. The reactor was placed in the 100 kHz coil and the power was adjusted to reach the temperature ~220°C. For security reasons, the reactive gas mixture (H_2/CO_2 – 1:4 v/v ratio, H_2 flow = 100ml min^{-1}, and CO_2 flow = 25 mL min^{-1}, GHSV = 7500 mL g_{cat}^{-1} h^{-1}) was passed through the reactor during day time (~9 h each day). At night the reactive gas mixture (H_2 and CO_2) switched to argon and the coil remains turned on at a constant power throughout the manipulation.

ASSOCIATED CONTENT

Supporting Information

Additional characterization data for commercial supports and as prepared catalyst, additional experimental procedures, additional catalytic tests data and analysis, magnetic property analysis data for as prepared and spent catalyst, and spent catalyst characterization data.

Author Contributions

‡These authors contributed equally.

Conflicts of interest

The authors declare no conflict of interest.

Acknowledgments

Authors gratefully acknowledge the funding from the ERC Advance grant (MONACAT 2015-694159). Authors thank Dr. Jaime Mazario (LPCNO, INSA Toulouse) for his valuable suggestions.

References

1. G. Liobikiene, M. Butkus, *Renew. Energy.* **2017**, *106*, 298-309.

2. G. Centi, E. A. Quadrelli, S. Perathoner, *Energy Environ. Sci.* **2013**, *6*, 1711-1731.

3. M. Younas, L. L. Kong, M. J. K. Bashir, H. Nadeem, A. Shehzad, S. Sethupathi, *Energy Fuels* **2016**, *30,* 8815–8831.

4. C. Vogt, M. Monai, G. J. Kramer, B. M. Weckhuysen, *Nat. Catal.* **2019**, *2*, 188–197.

5. G. Gahleitner, *Int. J. Hydrog. Energy* **2013**, *38,* 2039-2061.

6. P. Collet, E. Flottes, A. Favre, L. Raynal, H. Pierre, S. Capela, C. Peregrina, *Appl. Energy* **2017**, *192*, 282-295.

7. V. Rudnev, D. Loveless, R. L. Cook, *Handbook of induction heating,* CRC Press, New York, **2017**.

8. O. Lucia, P. Maussion, E. J. Dede, J. M. Burdio, *IEEE Trans. Ind. Electron.* **2014**, *61*, 2509-2520.

9. M. Banobre-Lopez, A. Teijerio, J. Rivas, *Rep. Pract. Oncol. Radiother.* **2013**, *18*, 397-400.

10. A. Meffre, B. Mehdaoui, V. Connord, J. Carrey, P.-F. Fazzini, S. Lachaize, M. Respaud, B. Chaudret, *Nano Lett.* **2015**, *15, 5*, 3241–3248.

11. A. Bordet, L.-M. Lacroix, P.-F. Fazzini, J. Carrey, K. Soulantica, B. Chaudret, *Angew. Chem. Int. Ed.* **2016**, *55*, 15894-15898.

12. W. Wang, C. Duong-Viet, Z. Xu, H. Ba, G. Tuci, G. Giambastiana, Y. Liu, T. Truong-Huu, J-M. Nhut, C. Pham-Huu, *Catal. Today* **2020**, *357*, 214-220.

13. J. Marbaix, N. Mille, L.-M. Lacroix, J. M. Asensio, P.-F. Fazzini, K. Soulantica, J. Carrey, B. Chaudret, *ACS Appl. Nano Mater.* **2020**, *3,* 3767–3778.

14. F. Varsano, M. Bellusci, A. La Barbera, M. Petrecca, M. Albino, C. Sangregorio, *Int. J. Hydrog. Energy* **2019**, *44*, 21037-21044.

15. M. G. Vinum, M. R. Almind, J. S. Engbaek, S. B. Vendelbo, M. F. Hansen, C. Frandsen, J. Bendix, P. M. Mortensen, *Angew. Chem. Int. Ed.* **2018**, *57*, 10569-10573.

16. I. Mustieles Marin, D. De Masi, L.-M. Lacroix, P.-F. Fazzini, P. W. N. M. Van Leeuwen, J. M. Asensio, B. Chaudret, *Green Chem.* **2021**, *23*, 2025-2036.

17. D. De Masi, J. M. Asensio, P.-F. Fazzini, L.-M. Lacroix, B. Chaudret, *Angew. Chem. Int. Ed.* **2020**, *59*, 6187-6191.

18. W. Wang, G. Tuci, C. Duong-Viet, Y. Liu, A. Rossin, L. Luconi, J-M. Nhut, L. Nguyen-Dinh, C. Pham-Huu, G. Giambastiani, *ACS Catal.* **2019**, *9*, 7921–7935.

19. A. Fache, F. Marias, B. Chaudret, *Chem. Eng. J.* **2020**, *390*, 124531.

20. S. Faure, S. S. Kale, N. Mille, S. Cayez, T. Ourlin, K. Soulantica, J. Carrey, B. Chaudret, *J. Appl. Phys.* **2021**, *129*, 044901.

21. L. M. Martínez-Prieto, J. Marbaix, J. M. Asensio, C. Cerezo-Navarrete, P.-F. Fazzini, K. Soulantica, B. Chaudret, A. Corma, *ACS Appl. Nano Mater.* **2020**, *3,* 7076–7087.

22. K. Stangeland, K. Dori, H. Li, Z. Yu, *Energy Procedia* **2017**, *105*, 2022-2027.

23. P. Frontera, A. Macario, M. Ferraro, P. Antonucci, *Catalysts* **2017**, *7*(2), 59.

24. Z. Bian, Y. Meng Chan, Y. Yu, S. Kawi, *Catal. Today* **2020**, *347*, 31-38.

25. H. Dong, Q. Liu, *ACS Sustainable Chem. Eng.* **2020**, *8,* 6753–6766.

26. J. Tan, J. Wang, Z. Zhang, Z. Ma, L. Wang, Y. Liu, *Appl. Surf. Sci.* **2019**, *481*, 1538-1548.

27. L. Shen, J. Xu, M. Zhu, Y.-F. Han, *ACS Catal.* **2020**, *10,* 14581–14591.

28. W. Gac, W. Zawadzki, M. Rotko, M. Greluk, G. Slowik, G. Kolb, *Catal. Today* **2020**, *357*, 468-482.

29. A. Quindmil, U. De-La-Torre, B. Pereda-Ayo, A. Davo-Quinonero, E. Bailon-Garcia, D. Lozano-Castellao, J. A. Gonzales-Marcos, A. Bueno-Lopez, J. R. Gonzalez-Velasco, *Catal. Today* **2020**, *356*, 419-432.

30. Z. J. Díaz-Puerto, A. Raya-Barón, P. W. N. M. van Leeuwen, J. M. Asensio, B. Chaudret, *Nanoscale* **2021**, *13*, 12438-12442.

31. W. Wang, C. Duong-Viet, G. Tuci, Y. Liu, A. Rossin, L. Luconi, J. M. Nhut, L. Nguyen-Dinh, G. Giambastiani, C. Pham-Huu, *ChemSusChem* **2020**, *13*, 5468-5479.

32. C. Niether, S. Faure, A. Bordet, J. Deseure, M. Chatenet, J. Carrey, B. Chaudret, A. Rouet, *Nat. Energy* **2018**, *3*, 476–483.

33. A. C. Ince, C. O. Colpan, A. Hagen, M. F. Serincan, *Fuel* **2021**, *304*, 121354.

34. M. R. Almind, S. B. Vendelbo, M. F. Hansen, M. G. Vinum, C. Frandsen, P. M. Mortensen, J. S. Engbaek, *Catal. Today* **2020**, *342*, 13-20.

35. J. M. D. Coey, *Magnetism and Magnetic Materials,* Cambridge University Press, Cambridge, **2010**.

36. J. Gao, Y. Wang, Y. Ping, D. Hu, G. Xu, F. Gu, F. Su, *RSC Advances* **2012**, *2*, 2358–2368.

10.1002/cssc.202201724

Table of contents entry:

Highly energy efficient and dynamic CO_2 methanation was achieved using supported nickel catalysts and commercial iron wool under induction heating conditions and in continuous flow mode